Numerical modeling of self-sealing in fractured clayey materials

Adriana Quacquarelli, Jean Talandier, Alice Di Donna, Frédéric Collin

Numerical modeling of self-sealing in fractured clayey materials

Adriana Quacquarelli[a], Jean Talandier[b], Alice Di Donna[c], Frédéric Collin[a]

[a] Urban and Environmental Engineering Research Unit, University of Liège, 4000 Liège, Belgium
[b] Andra, R&D Division, 92298 Chatenay-Malabry, France
[c] Univ. Grenoble Alpes, CNRS, Grenoble INP, 3SR, 38000, Grenoble, France

ABSTRACT

The excavation of underground research facilities (URF) in potential host rocks for nuclear waste disposals generates damage and fractures around the tunnels, defining an altered Excavation Damage Zone (EDZ). This fractures network can induce stress redistribution and alteration of flow and transport properties, becoming preferential paths for releasing radionuclides into the host rock. Nevertheless, in the long term, the fracture can be sealed through the resaturation of water coming from the rock as a function of its self-sealing potential, i.e., its capacity to restore its hydraulic permeability leading to the hydraulic closure of the fracture. The French National Agency for nuclear waste management (ANDRA) selected the Callovo Oxfordian Claystone (COx) as a potential host rock for its particular hydromechanical properties, such as its low permeability and high retention capacity of radionuclides. Several studies showed the self-sealing potential of COx claystone. The major contribution to this self-sealing capacity is given by the presence of clay minerals in its compositions, which are able to swell during water re-saturation. This process is quite fast; at the beginning, it involves mainly the zone just surrounding the fracture, leading to its rapid closure and, thus, a rapid reduction of water permeability. Moreover, this phenomenon is generally associated with the generation of microcracks around the fracture, where the material saturates quickly. In a second time, the sealing process progressively spreads out through the sample. This study aims to offer a unified constitutive model able to reproduce the self-sealing capacity of clay rocks. Implementing such a model in the finite element code LAGAMINE allowed its validation through comparison with laboratory tests. In particular, the role of the initial fracture size and the evolution of water permeability during the wetting/drying process was investigated, reproducing what has been observed experimentally.

1. Introduction

One of the major issues related to nuclear energy production is storing radioactive wastes. A modern and fair reasonable solution consists of sealing them in metal canisters and then storing them in repositories buried deeply in geological formations, ensuring the protection of people and the environment [1]. In this context, the tunneling and storage operations induce stress redistribution, triggering some damage to the host rock and generating an interconnected fractures network localized in the immediate vicinity of the gallery. This

altered zone is defined as Excavation Damage Zone (EDZ); it is characterized by hydro-mechanical and geochemical modifications responsible for altering the flow and transport properties of the host material locally, therefore reducing its safety function [2][3]. It was observed that the hydraulic conductivity of this zone could increase by several orders of magnitude during excavation [4]. The generated fractures could then become preferential pathways for the potential release and migration of radionuclides along the tunnels. Moreover, the air ventilation carried out in the gallery during the excavation and the operational phases could further fracture the host rock, altering its transport properties by increasing its permeability [5].

A damaged zone around the gallery can occur in any geological formation; nevertheless, the level of damage depends on the hydro-mechanical properties of the host rock, the in-situ stress field, the geometry of the opening, the excavation method, and its duration [6]. In this context, clay formations are considered suitable for hosting nuclear waste and have been extensively studied in different countries for their properties, such as low hydraulic conductivity and high retention capacity of radionuclides. In-situ experiments have been realized in Underground Research Laboratories (URLs) in different clay formations such as the Callovo-Oxfordian claystone (COx) in Bure in France (about 300 km east of Paris) [7], the Boom Clay in Mol in Belgium [2] and the Opalinus Clay in Mont Terri in Switzerland [8].

Moreover, once the gallery is closed and after the emplacement of wastes, fractures can be sealed through resaturation by the water coming from the claystone (Fig. 1) thanks to its self-sealing potential, i.e., the rock's capacity to swell, promoting the hydraulic closure of the fracture and helping in recovering its hydraulic permeability [2]. During this self-sealing process, local structural changes are observed, leading to fracture closure, but there is no mechanical strengthening. The interfaces remain a weakness plane in the material.

The self-sealing process proves to be a relevant feature in evaluating the potential host rock for nuclear waste disposal. For this reason, many experimental studies have been carried out to better understand and quantify it in the above-mentioned clay formations; the most relevant are summarized in [6]. At the laboratory scale, it was observed that the main mechanisms responsible for self-sealing are the swelling of clay minerals, consolidation, and creep [2].

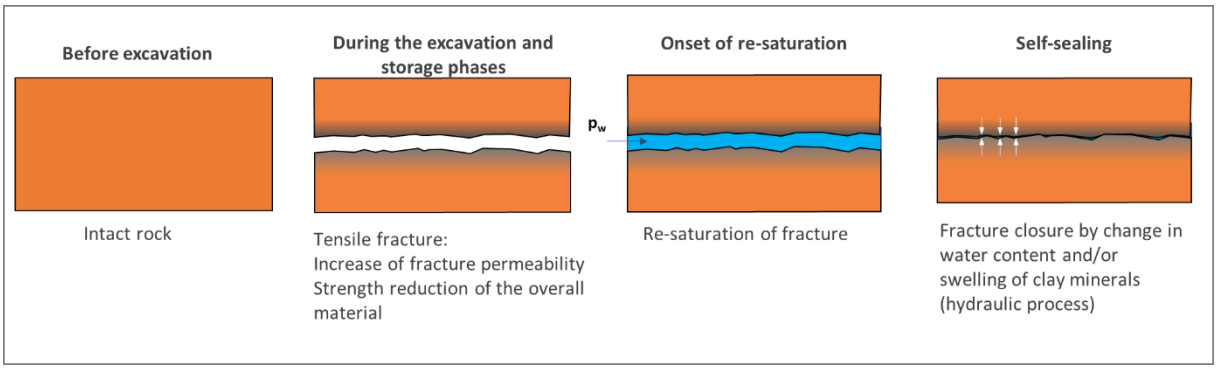

Fig. 1 Schematization of the self-sealing process involving the host rock close to the gallery

For instance, the Boom Clay was observed to seal faster than the Opalinus Clay. In both cases, the final permeability was very close to the undisturbed one. Moreover, in Boom clay, around

the original fracture, an area of lower density than the intact material and proportional to the size of the original fracture was observed [2], [9], [10].

Other experimental campaigns were conducted to understand and quantify the self-sealing of COx formation, both at the repository scale [11], [12] and on laboratory samples [13]–[18]. Since this paper deals essentially with self-sealing in COx samples, some of the experimental tests considered representative by the authors will be described in detail. The Callovo-Oxfordian claystone is a low-permeability claystone formation ($k_w \cong 10^{-20}\ m^2$) [19] consisting of three different geological units lying at a depth from 422 to 554 m [20]. More specifically, the French URL is built at 490 m depth in the lower unit, i.e., the argillaceous unit (U.A.), which consists mainly of phyllosilicates, in particular layers of illite (non-swelling clay) alternating with layers of smectite (swelling clay). The upper unit is the silt-carbonate unit (USC), while between them, there is a transitional unit (U.T.) with mineralogical properties between the two others [19]. The contribution of mineralogical composition (submicron scale) to the self-sealing capacity of the COx argillite is demonstrated by several laboratory tests [15]–[18]: samples taken from the carbonate-rich unit (USC) have a more limited self-sealing capacity compared to the clay-rich unit (U.A.). Therefore, the swelling of clay minerals plays a major role in the recovery of hydraulic properties. Conversely, the presence of a high carbonate content prevents water from penetrating the sample and swelling the clay minerals.

It has been shown that swelling of clay minerals begins in the areas around the fracture and then progressively spreads throughout the sample [21]. More specifically, a fracture results in an initial equivalent permeability of several orders of magnitude greater than intact clay. Then, during hydration and water uptake by the sample, the swelling process is quite rapid, leading to a rapid fracture closure and, thus, a rapid reduction in permeability. Finally, as it involves clay minerals far from the fracture, the process becomes slower and slower until it stabilizes. This phenomenon has been observed by several experimental campaigns, as summarized in Fig. 2 in terms of the temporal evolution of water permeability k_w.

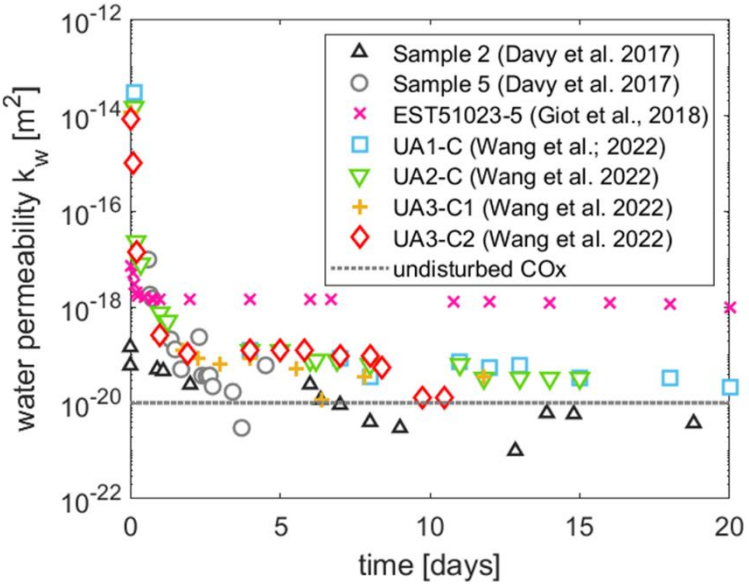

Fig. 2 Temporal evolution of water permeability k_w observed experimentally during hydration tests

The swelling and clogging of clay minerals define some microstructural changes around the fracture. A density lower than that of the intact material was observed in sealed COx samples [15], similar to what was observed in Boom Clay. This process is due to the fact that, during hydration, a pattern of secondary fractures is generated around the main one ([21], [22]), defining a disturbed and weak zone (i.e., low-density zone) (Fig. 3), which contributes significantly to the self-sealing of the claystone.

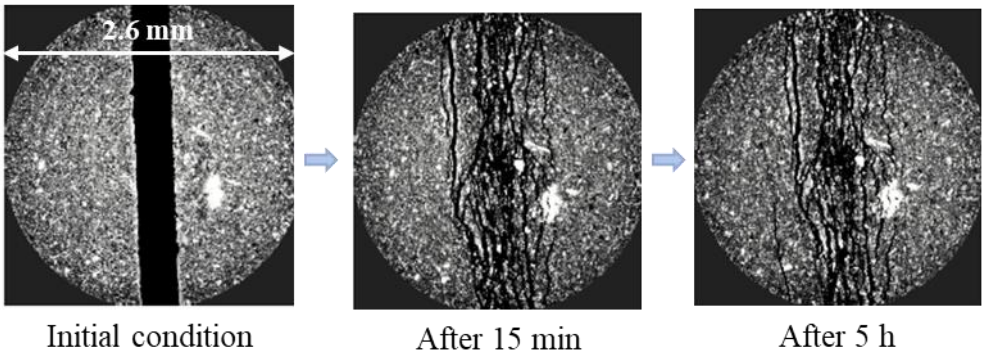

Fig. 3 X-ray images of a fractured Callovo – Oxfordian cylindrical sample (horizontal sections) at different time steps of a hydration test from the beginning (left) to the end (right) of the test [21]

Another aspect that has been investigated by laboratory testing is the role of the initial size of the fracture. In particular, the smaller the fracture, the faster it will close, despite the reduced peeling effect around it and thus the swelling capacity of the clay [21].

Although experimental results have shown that self-sealing is closely related to clay swelling caused by hydration, it is worth noting that many experiments are conducted under certain confining pressures [13], [14], [18] that contribute to the phenomenon, thus making it difficult to separate the role of clay mineral swelling from that of applied pressure.

Nevertheless, self-sealing has been extensively studied experimentally, but, to the authors' knowledge, limited attempts were made to model this phenomenon numerically. A numerical approach in this field is necessary to describe and understand the hydro-mechanical behavior of the fracture during hydration and drying through suitable constitutive laws able, in turn, to predict the self-sealing process in the long term. Wang and co-authors [23] proposed an elastoplastic damage model to describe self-sealing both at the sample scale and at the scale of the excavation damaged zone, i.e., the scale of the CDZ (Compression Damage Zone) experiment performed in Andra's URL. This model successfully describes the self-sealing of fractured unsaturated claystone; however, it does not define a constitutive model for the fracture.

This paper aims to offer a constitutive model that accounts for the claystone's sealing capacity, including some aspects introduced above (i.e., the clay swelling around the fracture and the initial size of the fracture). Then, this law is implemented in a finite element code and validated against some laboratory tests on COx samples under pseudo-oedometric conditions. This study is therefore propaedeutic for a more realistic large-scale model able to represent and predict self-sealing at the scale of the gallery. In the proposed model, the anisotropy of the material, but also the chemical properties of the saturation water are not considered. They both

deserve to be considered in future extension of the model. As will be seen below, this model aims to simulate a vertical section of the samples tested in the laboratory, and it is defined in 2D. This simplification is justified because the selected laboratory tests are carried out on cylindrical samples with a planar fracture, but future developments could also include the third dimension. The next Section 2 is dedicated to analyzing the already published experimental results, focusing on the key aspects responsible for the recovery of the hydraulic properties of the claystone. Then, Section 3 describes the numerical background, with particular attention paid to an interface constitutive model that can properly consider the observations reminded in Section 2. Section 4 deals with the construction of the numerical model as well as the numerical simulations, whose results are compared with experiments to validate the law. A general discussion is given in Section 5, while some conclusions are provided in the final Section 6.

2. Mechanisms contributing to the self-sealing of fractures during hydration

The experimental campaign published in [21] investigated the role of clay content during the self-sealing of COx claystone. Different samples with different initial fracture openings were prepared from the same core extracted from the U.A. The hydration test consisted in injecting water within the fracture. From the mechanical point of view, the samples were not loaded but kept in pseudo-oedometric conditions (lateral strain prevented). Then, through Digital Volume Correlation (DVC), it was possible to monitor the strain and displacement fields during the test and thus follow the closure of the fracture during hydration. For the experimental developments and the image analysis, the reader should refer to the published works [16], [21]. In this study, the most relevant conclusions are considered to provide a suitable constitutive law for the fracture that includes the physical mechanisms responsible for its hydraulic closure. When saturation starts, it was observed that it first involves the clay minerals close to the fracture, which swell and tend to close the discontinuity quickly. This aspect is displayed in Fig. 4(a) (images W1-W6), where displacements concentrate around the fracture lips, and their sign is consistent with the fracture closure (Fig. 4(b)). Then the saturation progressively involves the whole sample (Fig.4(a); W7-W10) until a final condition in which the swelling is prevented at the outer borders constrain.

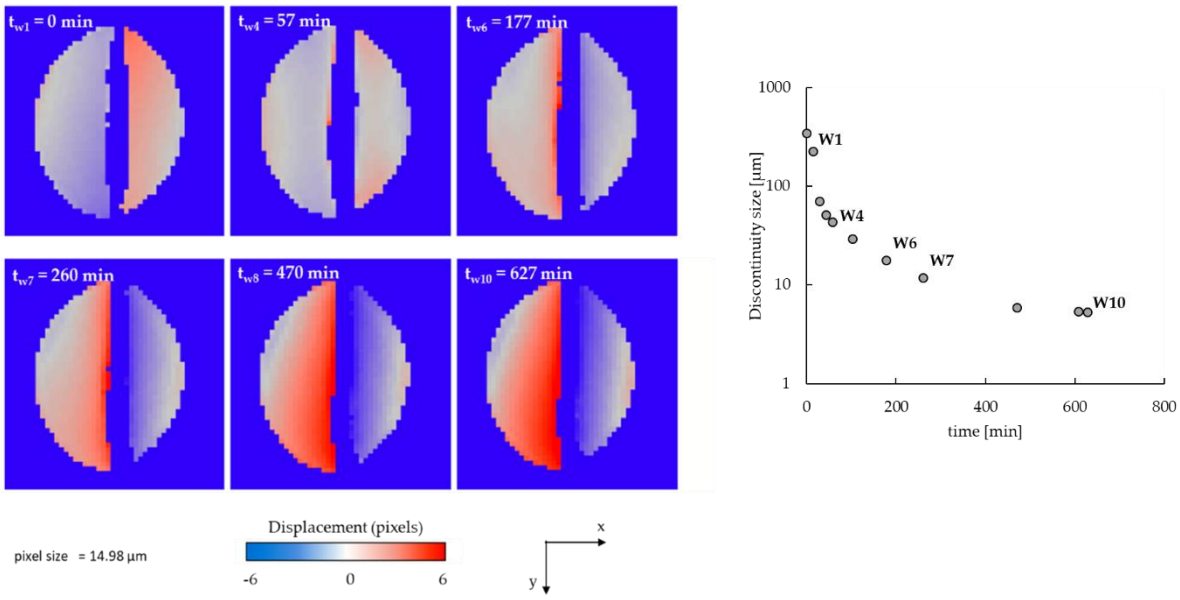

(a) (b)

Fig. 4 (a) X Displacement fields resulted from DVC for a cylindrical sample (n. 8182) of diameter 8 mm, averaged over the sample height for different time lapses t_{wi}; (b) Evolution of the discontinuity size with time [21]

The rapid swelling in the proximity of the fracture is associated with the generation of parallel micro-cracks around the main one (Fig. 5(a)). This fracture network defines a damaged zone and contributes to the recovery of the hydraulic properties. Moreover, it was observed that the size of this fractured zone is related to the initial size of the discontinuity: the smaller the initial fracture aperture, the smaller the space available for deformation, and the smaller the fractured area is.

To further investigate self-sealing, Fig. 5(a) allows the measurement of the thickness of the damaged zone (i.e., the zone including the main fracture and sub-fractured sides). Then, subtracting the size of the main discontinuity (already measured in [21]) gives the thickness of the damaged sides. Finally, for practical reasons, a symmetrical micro-cracks network is assumed, such that the thickness computed previously can be divided by 2 to obtain the thickness of each damaged side at the beginning of hydration h_{ini}. This thickness is plotted against the initial size of the fracture d_{ini} in Fig. 5(b), for each hydration test of Fig. 5(a). Finally, results can be fitted by an empirical power law type that can be assumed representative of COx samples with planar fracture. This relationship is consistent with experimental evidence since its sides remain intact ($h_{ini} \to 0$) if the initial fracture is sufficiently small ($d_{ini} \to 0$).

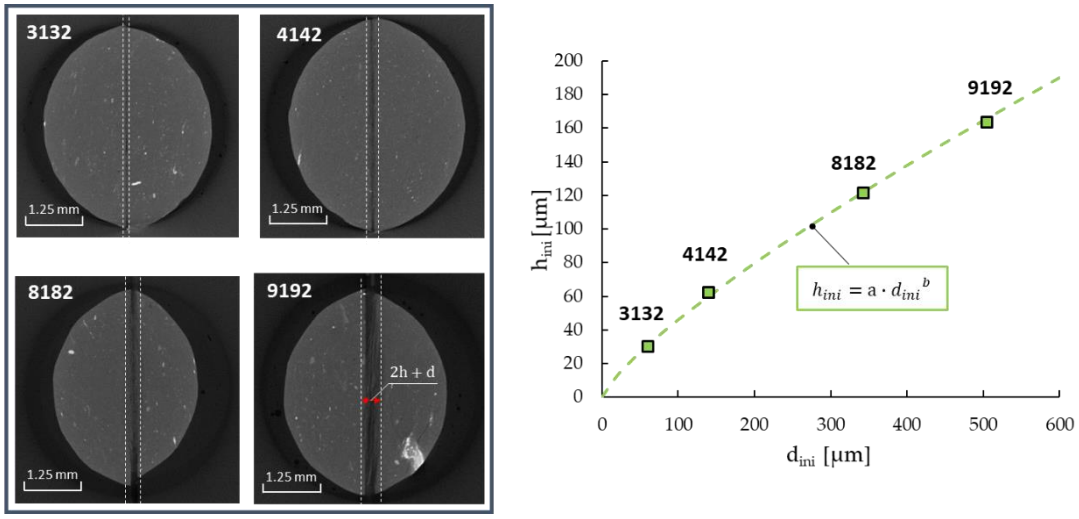

(a) (b)

Fig. 5 (a) X-ray images after a few minutes of hydration, middle slice [21] with the definition of the interface zone in the middle of the section (white dashed line) including the fracture and the damaged sides; (b) Definition of the initial extension of the damaged sides ($h_{1,ini} = h_{2,ini} = h_{ini}$) in relation with the initial size of the fracture d_{ini} fitted by a power law type (a = 1.2019; b = 0.7914 R^2 = 0.9989)

3. Theoretical formulation for the fracture and the intact material

The self-sealing of the claystone is investigated numerically by a 2D isothermal model implemented in the finite element code LAGAMINE [24], [25]. The intact clay is modeled in the framework of the continuum mechanics and is assumed as a linear elastic material, while the fractured zone is modeled using a zero-thickness interface element [26]–[28]. This interface element is widely used in modeling joints and rock discontinuities in the framework of finite element methods since it is suitable for large deformations without re-meshing. It has also been used to model the interface between two different media [29], [38], as well as in rock fracture mechanics [39].

The contact zone is discretized through field nodes and is only activated in the case of contact. An accurate description of this type of contact element is provided by Cerfontaine et al. [29] for a 3D problem, while a 2D schematization is given in Fig. 6(a). The zero-thickness element is discretized by the three-node method, i.e., the interface element includes the inner of the discontinuity (index F) and the two adjacent sides (indexed Γ^1 and Γ^2) allowing the modeling of the fluid flow propagation along and through the discontinuity (f_l and f_{ti} in Fig. 6(b)). Each node of the two sides (i.e., nodes 1-6) carries 3 degrees of freedom (the displacements u_x and u_y in the horizontal and vertical direction, respectively, and the pore water pressure p_w). Each inner node (i.e., nodes 1'-3') is fixed in terms of displacement and thus carries only the pore water pressure degree of freedom.

This discretization allows a homogenous field of pressure across the interface while there is a transversal drop of pressure between the two sides of the fracture [29]. The fracture opening d in Fig. 6(b) is measured as the distance between the nodes of the side Γ^1 and those of Γ^2 and is computed through a segment-to-segment discretization [30]–[32] as described in [29].

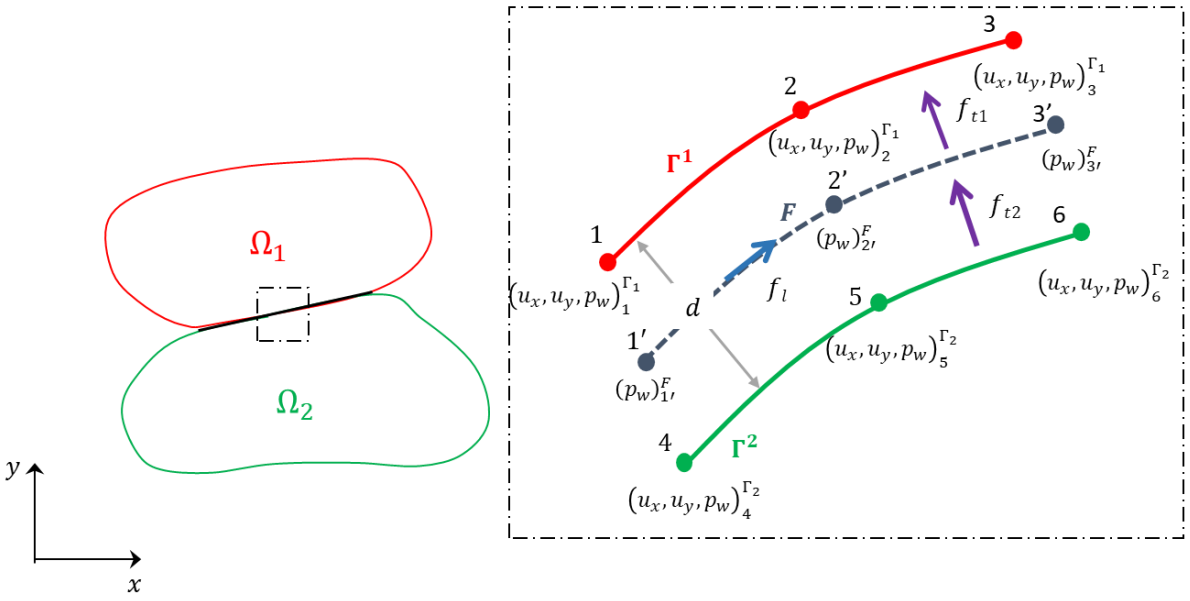

(a) (b)

Fig. 6 (a) Contact between two continuum deformable solids Ω_1 and Ω_2; (b) Definition of the parabolic three-node discretization of an interface element where Γ_1 and Γ_2 are the side of the interface (nodes 1-6), F is the inner of the interface (nodes 1′-3′ obtained as the projection of nodes 1-3 of the side Γ_1)

3.1. The hydro-mechanical formulation for the fracture

3.1.1. The mechanical problem

The fracture mechanical behavior is defined in terms of variation of the contact pressure with the fracture closure V (or the hydraulic aperture d). When two perfectly smooth continuum elements are not in contact, the closure V takes positive values. If the two parts come into contact, their contact pressure increases while the distance V between them cancels (yellow curve in Fig. 7). Nevertheless, the two counterparts are never perfectly smooth, but some roughness on contact area exists. Since it is not possible to model all the asperity by finite elements, the two adjacent surfaces are assumed to be perfectly smooth, and the average distance between them defines the fracture closure V. In the particular case of rock joints, a non-linear contact law accounting for the role of the asperities in contact was experimentally observed [26], [33]–[36]. Among the others, a recent formulation to describe the non-linear mechanical behavior of the fracture was proposed by Bart [37] and is represented in Fig. 7 (in blue) in terms of effective normal pressure p'_N. In the incremental form it writes:

$$\Delta p'_N = -\frac{\widetilde{K}_N}{\left(1+\frac{V}{D_0}\right)^{\gamma}}\Delta V \tag{1}$$

D_0 defines the asymptotic mechanical closure of the fracture in absolute value, $\widetilde{K}_N$ is the stiffness coefficient defining the initial slope of the curve (for small values of p'_N) and the exponent γ is a correction factor taken equal to 2 to represent the fracture behavior better but generally varying between 2 and 6 [33].

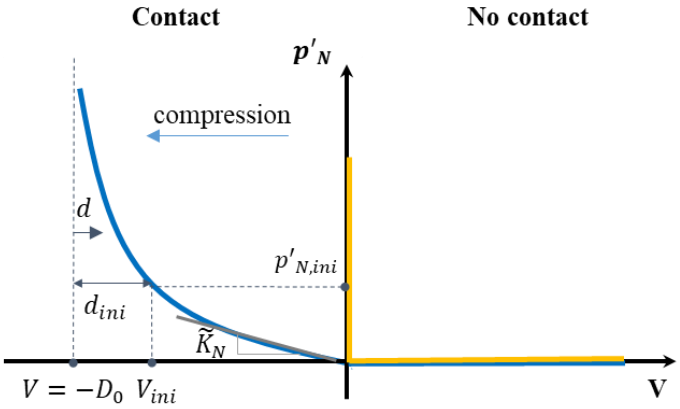

Fig. 7 Interface normal behavior in terms of fault closure V – effective normal contact pressure p'_N in the ideal case of a smooth interface (in yellow) and the real one of a rough interface (in blue). The values V_{ini}, d_{ini} and $p'_{N\,ini}$ indicates the closure, hydraulic aperture and the contact pressure, respectively at the beginning of the test

If two bodies initially not in contact get closer and closer, their asperities begin to touch and deform, with large displacement for low applied stress. This behavior is described through the initial slope $\widetilde{K}_N$ defining a linear relationship between the normal contact pressure and the closure. Then, the applied stress progressively induces smaller and smaller deformations since the fracture is closing more and more, and the number of asperities in contact increases. At this stage, the interpenetration of the two counterparts is related to the contact and deformation of asperities. The pressure-closure relationship is no more linear and is defined by the normal stiffness:

$$K_N = \frac{\widetilde{K}_N}{\left(1 + \frac{V}{D_0}\right)^{\gamma}} \tag{2}$$

It depends on the mechanical properties of the rock, the physical properties of the filling material (if any), and the configuration of the asperities (i.e., the number, surface, and relative position). In this study, it should be intended as a penalty parameter introduced to ensure the constraint of normal contact allowing the two contacting surfaces to interpenetrate each other to simulate the contact between asperities. It should be high enough to avoid artificial overlap between the two counterparts keeping in mind that too large values can ill-condition the problem. Finally, the fracture behavior can be compared with the intact rock for a given load applied. This occurrence explains the asymptote D_0 corresponding to the maximum mechanical closure of the fracture.

From Fig. 7, the hydraulic opening d and closure V are related to each other by the relationship:

$$D_0 = |d| + |V| = |d_{ini}| + |V_{ini}| \tag{3}$$

The index $-ini$ indicates the initial values at the beginning of the test. Knowing the initial hydraulic aperture d_{ini}, the slope $\widetilde{K}_N$ and the normal contact stress p'_N at the beginning of the test, D_0 is computed by coupling Eq. (3) with:

$$V_{ini} = D_0 \left[\sqrt[1-\gamma]{\left(\frac{(1-\gamma)}{D_0 \widetilde{K}_N} p'_{N,ini} + 1 \right)} - 1 \right] \tag{4}$$

The opening d is always positive, while the closure V can be either positive (no contact) or negative (contact).
Finally, the following statements apply:

- If there is no contact, the hydraulic closure V is zero, while the hydraulic opening d is equal to the mechanical asymptotic closure D_0 ($p'_N = 0 \rightarrow V = 0$ and $d = D_0$);
- If the contact pressure reaches large values, then the hydraulic closure V reaches mechanical asymptotic closure D_0, while the hydraulic opening d becomes null ($p'_N = \infty \rightarrow V = D_0$ and $d = 0$).

3.1.2. The fluid flow problem

The three-node discretization introduced above allows the description of the fluid flow (e.g., water in this particular case study) considering as a variable the pore water pressure inside the interface and on the two sides in contact. In this way, it is possible to calculate the longitudinal flow along the discontinuity and the transverse flow inside the interface (Fig. 6).

Flow equations along the fracture

The liquid water flow along the discontinuity is described by Darcy's equation:

$$q_l = -\frac{k_{r,w}^{(F)} k_w^{(F)}}{\mu_w} \nabla p_w^{(F)} \tag{5}$$

The index F stays for the fracture, μ_w is the water dynamic viscosity, ∇p_w is the gradient of pore water pressure, $k_{r,w}$ and k_w are the relative and intrinsic permeability of the fracture. Since the fracture saturate quickly during water injection, the relative value $k_{r,w}$ is set to the unit value, hence the permeability is defined by the intrinsic value k_w that varies with the fracture opening.

Water retention curve

The unsaturated behavior of a material is described by its water retention curve. In this case, since the two damaged sides are very narrow, they are assumed to follow the same flow equations and retention curve as the intact material. To the authors' knowledge, there are no experimental investigations on the retention properties of the discontinuities. In this study, it is assumed that the water retention curve inside the discontinuity is represented by the Van Genutchen relation [40]:

$$S_{r,w}^F = \left(1 + \left(\frac{s^F}{p_a^F}\right)^{m^F}\right)^{\frac{1}{m^F}-1} \tag{6}$$

Where $S_{r,w}$ is the degree of saturation; s (i.e.: $p_g - p_w$) is the suction; p_a^F and m^F are, respectively, the air entry pressure and the shape coefficient of the curve. More specifically, the air entry pressure is the suction value at which pore water starts to displace from the initially saturated condition. Therefore, the higher the fracture opening d and the smaller should be the threshold p_a^F. The Laplace equation accounts for this aspect:

$$p_a^F = \frac{2\sigma}{d} \tag{7}$$

Where σ is the water tension surface ($\sigma = 0.073\ N/m$). As already said, in this study, the fracture is initially unsaturated and should rapidly become saturated during the hydration phase. This behavior can be considered by choosing a relatively high value for the shape coefficient m^F in Eq.(6) (compared to the one describing the intact material defined in Section 3.2), bearing in mind that too large values can cause numerical convergence issues.

Flow equations across the fracture

Water can also flow through the two adjacent surfaces as a function of the transversal permeability of the fractured material (i.e., the transmissivity) and the difference in pressure between the discontinuity and its two counterparts. According to Fig. 6, the two transversal flow writes:

$$\begin{aligned} f_w^{t1} &= \rho_w T_w^1 t_{rw}^1 \left(p_w^{(F)} - p_w^{(\Gamma^1)}\right) \\ f_w^{t2} &= \rho_w T_w^2 t_{rw}^2 \left(p_w^{(\Gamma^2)} - p_w^{(F)}\right) \end{aligned} \tag{8}$$

The transmissivity coefficient is defined as the product between the intrinsic and the relative value, i.e., T_w^i and t_{rw}^i, respectively. They depend on the fluid and rock properties and should be adequately calibrated.

The intrinsic transmissivity coefficient T_w^i is a constant of the material and must take into account the transfer between the fluid in the fracture and the two counterparts. When liquid water is considered, the transfer is faster than with vapour water because, in the latter case, some mass exchanges must occur at the wall of the counterparts. The relative value t_{rw}^i is a dimensionless parameter function of the degree of saturation, accounting for the water transmissivity in a two-phase flow (e.g., the water permeability in an unsaturated medium).

Since this case study deals with the contact between two continuums of the same material, the same coefficients are assumed for the two adjacent parts 1 and 2:

$$\begin{aligned} T_w^1 &= T_w^2 = T_w \\ t_{rw}^1 &= t_{rw}^2 = t_{rw} \end{aligned} \tag{9}$$

Water relative transmissivity curve

The relative transmissivity coefficient t_{rw} is related to the degree of saturation through the Van Genutchen equation [40]:

$$t_{rw} = \sqrt{S_{r,w}^F}\left(1 - \left(1 - {S_{r,w}^F}^{1/n^F}\right)^{n^F}\right)^2 \tag{10}$$

The shape coefficient n^F is related to the shape coefficient m^F of the fracture retention curve defined in Eq. (6): $n^F = 1/m^F - 1$.

In saturated conditions, the relative transmissivity assumes the unit value while it assumes values lower than one in the unsaturated case, thus reducing the total transmissivity coefficient during drying. This aspect is consistent with the fact that the gas propagates more slowly than water.

The main hydraulic parameters for the interface zone are synthesized in Tab. 1.

Tab. 1 Hydraulic parameters for the interface element

Parameter	*Symbol (unit)*	*Value*
Porosity	ϕ (%)	100
Tortuosity	τ $(-)$	1.00
Van Genutchen coefficient	m^F $(-)$	1.67
Van Genutchen coefficient	$n^F(-)$	0.401
Intrinsic transmissivity (water)	$T_w^i(m/Pa\ s)$	Calibrated
Intrinsic transmissivity (vapor)	$T_w^i(m/Pa\ s)$	Calibrated

3.1.3. *The hydro-mechanical coupling*

The hydraulic and mechanical formulations are coupled through the Terzaghi's effective stress principle under unsaturated conditions [41].

On the other side, the flow properties of the fracture are strongly dependent on its aperture by the mean of the cubic law, defining the fluid flow proportional to the cubic of the fracture opening d. By schematizing the fracture as two flat surfaces separated by a distance equal to the opening d and characterized by a unit thickness w (Fig. 8), Poiseuille's law defines the fluid flow rate Q as:

$$Q = \frac{w\, d^3}{12\mu_w} \frac{p_w^{out} - p_w^{in}}{L} \tag{11}$$

where p_w^{in} and p_w^{out} are respectively the inlet and the outlet pressure, and L is the fracture length.

Then, the Darcy equation writes:

$$Q = \frac{k_w^{(F)}\, A}{\mu_w} \frac{p_w^{out} - p_w^{in}}{L} \tag{12}$$

Where $A = dw$ is the area of the cross-section. Combining the Eqs. (11) and (12):

$$k_w^{(F)} = \frac{d^2}{12} \tag{13}$$

This equation is the expression of the cubic law correlating the water permeability of the fracture to its opening. Eq. (13) simplifies the reality as it does not consider roughness when assessing permeability. It has, however, been validated by several studies [42], [43]. In particular, roughness can be considered by referring to the hydraulic opening instead of the mechanical opening [44].

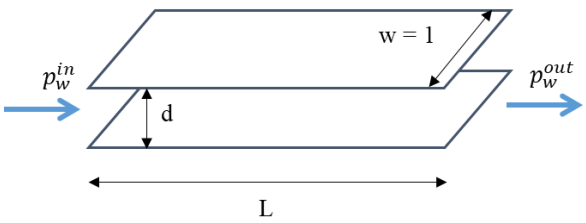

Fig. 8 Simplification of the fracture as two parallel plates with the definition of the inlet and outlet pressure (p_w^{in} and p_w^{out}, respectively)

The calculation of the hydraulic opening d during the resaturation process requires further

investigation. As reminded in Section 2, the hydration of the fracture induces some micro-cracks around it, defining a damaged zone able to swell quickly, favoring the hydraulic closure of the fracture. The thickness of this zone depends, for the same material, on the initial thickness of the fracture. Hence, since the area around the discontinuity contributes to self-sealing, it must be considered when describing the interface constitutive behavior.

The modeling of these damaged sides requires further numerical effort. Nevertheless, since they are narrow enough compared to the sample sizes (about the same order of magnitude as the fracture opening), they do not need to be explicitly meshed. This evidence allows us to implement them directly in the interface element with considerable numerical simplification, as illustrated in Fig. (9). This aspect is simulated numerically by including two deformable zones into the interface element, as shown in Fig. 9: the stiffness of the two sides, Γ_1 and Γ_2, are $K_N^{(\Gamma_1)}$ and $K_N^{(\Gamma_2)}$ respectively, while inside the interface, the stiffness is computed as defined in Eq. (2). Since the thickness of these damaged boundaries is relatively small, isotropic behavior is assumed whereby the stiffness moduli are derived from the modified Cam Clay model [45] and normalized by their initial thickness, i.e. $h_{1,ini}$ and $h_{2,ini}$ respectively:

$$\begin{cases} K_N^{(\Gamma_1)} = \dfrac{1}{h_{1,ini}} \left(\dfrac{1+e_{ini}}{\kappa_{el}^{(\Gamma_1)}} p'^{(\Gamma_1)}_{N,ini} \right) \\ K_N^{(\Gamma_2)} = \dfrac{1}{h_{2,ini}} \left(\dfrac{1+e_{ini}}{\kappa_{el}^{(\Gamma_2)}} p'^{(\Gamma_2)}_{N,ini} \right) \end{cases} \tag{14}$$

where e_{ini} is the initial void ratio, $p'^{ini(\Gamma_1)}_N$ and $p'^{ini(\Gamma_2)}_N$ are the reference effective mean pressures (assumed equal to the respective values at the beginning of the test) and $\kappa_{el}^{(\Gamma_1)}$ and $\kappa_{el}^{(\Gamma_2)}$ are the elastic coefficients, which should be calibrated numerically.

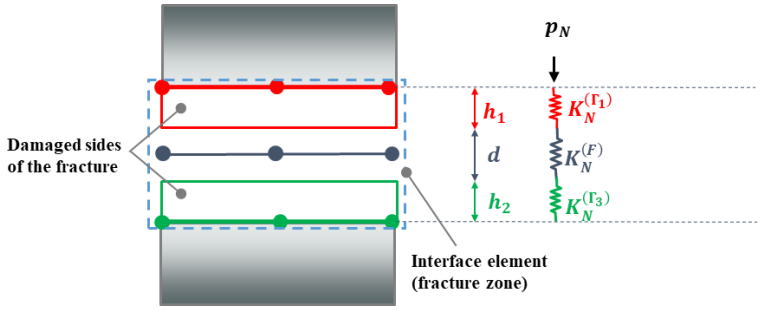

Fig. 9 Sketch of the interface element accounting for the damaged area around the main fracture

For the equilibrium, the total pressure is the same across the whole system and, therefore, in the interface element, the same increment of total normal stress Δp_N is applied:

$$\Delta p_N^{(\Gamma_1)} = \Delta p_N^{(\Gamma_2)} = \Delta p_N^{(F)} = \Delta p_N \tag{15}$$

By applying the Terzaghi effective stress principle, the equilibrium of the system can be written as:

$$\begin{cases} \Delta p_N = \Delta p'^{(\Gamma_1)}_N + S_{rw}^{(\Gamma_1)} \Delta p_w^{(\Gamma_1)} + \left(1 - S_{rw}^{(\Gamma_1)}\right) \Delta p_g^{(\Gamma_1)} \\ \Delta p_N = \Delta p'^{(\Gamma_2)}_N + S_{rw}^{(\Gamma_2)} \Delta p_w^{(\Gamma_2)} + \left(1 - S_{rw}^{(\Gamma_2)}\right) \Delta p_g^{(\Gamma_2)} \\ \Delta p_N = \Delta p'^{(F)}_N + S_{rw}^{(F)} \Delta p_w^{(F)} + \left(1 - S_{rw}^{(F)}\right) \Delta p_g^{(F)} \end{cases} \tag{16}$$

In the following, we will omit the terms $(1 - S_{rw})\Delta p_g$ since the gas pressure is kept constant

at environmental conditions in this numerical study.

The variation of effective normal pressure $\Delta p'_N$ is obtained assuming an elastic constitutive behavior for the whole interface element (i.e., inner fracture + damaged sides). In particular, the increment of the effective normal pressure inside the interface $\left(\Delta p'^{(F)}_N\right)$ can be related to the increment of the fault opening Δd, as well as the increment of the effective normal stress on the two sides Γ^1 and Γ^2 can be related to their swelling Δh_1 and Δh_2 respectively:

$$\begin{cases} \Delta p'^{(\Gamma_1)}_N = -K_N^{(\Gamma_1)} \Delta h_1 \\ \Delta p'^{(\Gamma_2)}_N = -K_N^{(\Gamma_2)} \Delta h_2 \\ \Delta p'^{(F)}_N = -K_N^{(F)} \Delta d \end{cases} \tag{17}$$

The negative sign indicates that the effective normal pressure is assumed positive in compression.

Finally, substituting Eqs. (17) in Eqs. (16), it is possible to find the amount of swelling of the fracture sides (Δh_1 and Δh_2) and the increment of the hydraulic opening Δd:

$$\begin{cases} \Delta h_1 = \dfrac{K_N^{(\Gamma_2)} K_N^{(F)} \Delta h_{TOT} - K_N^{(F)} \left(S_{rw}^{(\Gamma_1)} \Delta p_w^{(\Gamma_1)} - S_{rw}^{(\Gamma_2)} \Delta p_w^{(\Gamma_2)}\right) - K_N^{(\Gamma_2)} \left(S_{rw}^{(\Gamma_1)} \Delta p_w^{(\Gamma_1)} - S_{rw}^{(F)} \Delta p_w^{(F)}\right)}{K_N^{(\Gamma_2)} K_N^{(\Gamma_1)} + K_N^{(F)} K_N^{(\Gamma_2)} + K_N^{(F)} K_N^{(\Gamma_1)}} \\ \Delta h_2 = \dfrac{K_N^{(\Gamma_1)} K_N^{(F)} \Delta h_{TOT} - K_N^{(\Gamma_1)} \left(S_{rw}^{(\Gamma_2)} \Delta p_w^{(\Gamma_2)} - S_{rw}^{(F)} \Delta p_w^{(F)}\right) - K_N^{(F)} \left(S_{rw}^{(\Gamma_2)} \Delta p_w^{(\Gamma_2)} - S_{rw}^{(\Gamma_1)} \Delta p_w^{(\Gamma_1)}\right)}{K_N^{(\Gamma_2)} K_N^{(\Gamma_1)} + K_N^{(F)} K_N^{(\Gamma_2)} + K_N^{(F)} K_N^{(\Gamma_1)}} \\ \Delta d = \dfrac{K_N^{(\Gamma_1)} K_N^{(\Gamma_2)} \Delta h_{TOT} - K_N^{(\Gamma_1)} \left(S_{rw}^{(F)} \Delta p_w^{(F)} - S_{rw}^{(\Gamma_2)} \Delta p_w^{(\Gamma_2)}\right) - K_N^{(\Gamma_2)} \left(S_{rw}^{(F)} \Delta p_w^{(F)} - S_{rw}^{(\Gamma_1)} \Delta p_w^{(\Gamma_1)}\right)}{K_N^{(\Gamma_2)} K_N^{(\Gamma_1)} + K_N^{(F)} K_N^{(\Gamma_2)} + K_N^{(F)} K_N^{(\Gamma_1)}} \end{cases} \tag{18}$$

When the two fracture sides have an infinite bulk modulus ($K_N^{(\Gamma_1)} = K_N^{(\Gamma_2)} \to \infty$: i.e., a null elastic coefficient or a null thickness), the constitutive mechanical laws defined in Eqs. (17) reduces to the form defined in Eq. (1) where $\Delta V = \Delta d$.

Considering that the two claystone elements respond to the same constitutive behavior, the same material properties are assumed at the two disturbed zones around the fracture. They have the same initial thickness that can be computed as a function of the initial fracture aperture d as in Fig. 5(b) (i.e., $h_{1,ini} = h_{2,ini} = h_{ini}$) and the same elastic coefficients ($\kappa_{el}^{(\Gamma_1)} = \kappa_{el}^{(\Gamma_2)} = \kappa_{el}$) that should be adequately calibrated. Together with the penalty factor $\widetilde{K}_N^{(F)}$, they are properties of the material concerned independently from the test, the initial, and the boundary conditions. It is important that the ratio between the stiffness of the two disturbed zones and the penalty $K_N^{(F)}$ ensures the rapid hydraulic closure observed experimentally during wetting.

3.2. The hydro-mechanical formulation for the intact material

3.2.1. Mechanical problem

Since this study focuses on the discontinuity, the intact claystone is simply described as an isotropic linear elastic material.

The main mechanical parameters of the Callovo Oxfordian claystone have been provided by several experimental campaigns and are synthesized in Tab. 2.

Tab. 2 Mechanical parameters of Callovo-Oxfordian argillite (from [46])

Parameter	*Symbol (unit)*	*Value*
Dry density	$\rho_d\ (g/cm^3)$	2.21-2.34
Grain density	$\rho_s\ (g/cm^3)$	2.71
Young's modulus	$E\ (MPa)$	4000
Poisson's coefficient	υ (-)	0.3

As explained in the following, the claystone can be disturbed during the sample preparation, especially for small-size samples. In this case, a lower Young modulus should be considered.

3.2.2. *Flow problem*

As for the interface, the hydraulic constitutive behavior of the bulk material accounts for the advection of liquid water through Darcy's equation.

Water Retention Curve and relative permeability

The water retention curve of the Callovo Oxfordian claystone was obtained by fitting the available data with the van Genuchten equation [47], as shown in Fig. 10. During the drying process, gas displaces the water until residual saturation is reached. Then, during resaturation, some gas bubbles may be trapped in the interstitial space resulting in a lower degree of saturation than during the desaturation phase. This process explains the hysteretic behavior of the retention curves in Fig. 10. Furthermore, by definition, the air entry value is higher in the desaturation curve than in resaturation.

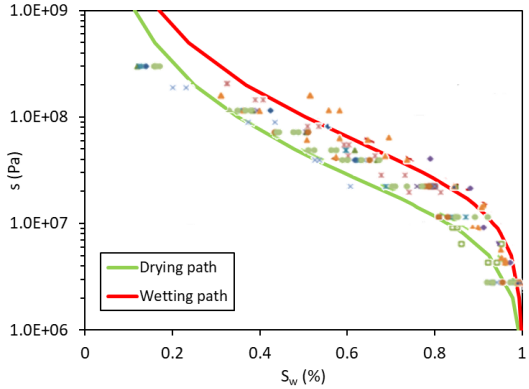

Fig. 10 Water retention curve for Callovo-Oxfordian claystone [47]

As already discussed for the fracture, the water flow through the claystone depends on its hydraulic permeability that varies, in unsaturated conditions, with the degree of saturation. Similarly to the relative transmissivity coefficient defined in Eq. (10), the van Genuchten formulation defines the relative permeability as a function of the degree of saturation for the intact claystone:

$$k_{r,w} = \sqrt{S_{r,w}}\left(1 - \left(1 - S_{r,w}^{1/n}\right)^n\right)^2 \tag{19}$$

The hydraulic parameters for the Callovo-Oxfordian claystone are listed in Tab. 3.

Tab. 3 Hydraulic parameters for the Callovo-Oxfordian claystone [47]–[49]

Parameter	*Symbol (unit)*	*Value*
Horizontal saturated water permeability	$k_{w,H}^{sat}\ (m^2)$	$3.40\ 10^{-20}$
Vertical saturated water permeability	$k_{w,V}^{sat}\ (m^2)$	$1.33\ 10^{-20}$
Porosity	$\phi\ (\%)$	$15\ -\ 18$
Water content	$w\ (\%)$	$3\ -\ 7$
Tortuosity	$\tau\ (-)$	0.25
Air entry value	$p_a\ (MPa)$	12
Van Genutchen coefficient	$m\ (-)$	1.49
Van Genutchen coefficient	$n\ (-)$	0.329

For the sake of simplicity, the hysteretic behavior of the retention curve is not considered in the modeling and only the wetting curve is considered. Moreover, the model is defined in isotropic conditions. For the test described hereafter, the fracture is vertical and oriented parallel to the bedding plane; thus, only vertical permeability is accounted for in the numerical model.

4. Numerical modeling

The hydro-mechanical modeling of fractured Callovo-Oxfordian claystone samples is performed in 2D plane strain conditions. The validation of the interface model requires the calibration of its parameters and the comparison with some laboratory tests. The following hydraulic paths are selected for this purpose:

- Wetting test [17]: water is injected into the fracture starting from the initial unsaturated condition;
- Water vapor - wetting – drying test [21]: the sample is firstly saturated by water vapor and then by liquid water, and finally, it is dried by injecting dry air;
- Drying–wetting test [21]: the sample is firstly dried and then re-saturated by injecting liquid water.

4.1. Model construction

All the experimental tests used for calibration and validation were conducted on cylindrical samples artificially fractured, as illustrated in Fig. 11(a). The sample was contained in a rigid shell to prevent lateral deformation. To assess only the effect of resaturation on the hydraulic recovery, no confining pressure was imposed. The sample fracture is oriented parallel to the bedding plane. Since the modeling was carried out in 2 dimensions, only a vertical slice of the sample was considered, as illustrated in Fig. 11(a), meaning that the anisotropy of the material is not taken into account. The geometry, mesh, and boundary conditions are schematized in Fig. 11(b). The sample dimensions and the initial thickness of the discontinuity are defined for each test in Sections 4.2-4.4. In all tests, the displacements normal to the external boundaries are fixed.

The two counterparts of the fracture are free to move, allowing swelling or contraction during the test. Then water is injected from one extremity of the fracture controlling the pressure while the other is set to environmental conditions ($p_w = 0.1\ MPa$). Depending on the test, the water pressure applied can be either positive or negative. Depending on the clay transmissivity, water can flow across the interface, permeate the fractured walls, and eventually saturate/de-saturate the entire system, generating a new equilibrium condition. The intrinsic transmissivity coefficient needs to be calibrated, while the other main hydraulic parameters of the fracture are listed in Tab. 1. Moreover, the calibration also involves the mechanical parameters of the fracture, i.e., the coefficient $\widetilde{K}_N$ of the discontinuity and the elastic coefficient κ_{el} of the two disturbed sides. The hydro-mechanical properties of the bulk material are defined in Tab. 2 and Tab. 3.

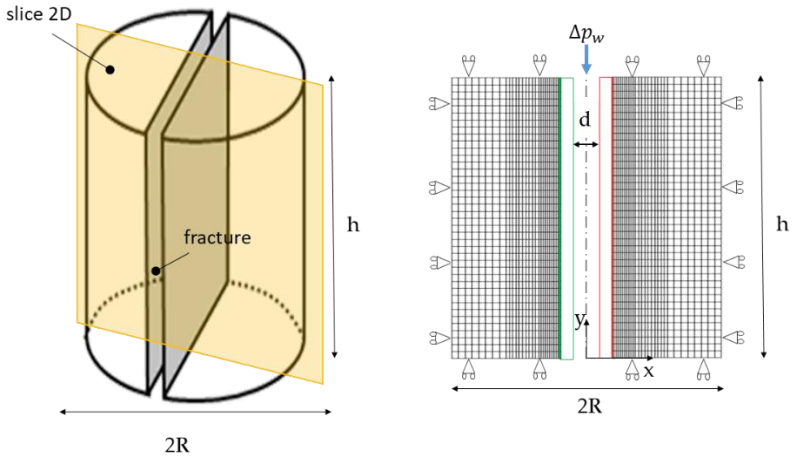

(a) (b)

Fig. 11 Construction of the model: (a) Sketch of a cylindrical sample prepared and fractured artificially, the vertical slice (in light yellow) is used for the 2D model building; (b) 2D model with the definition of mesh, boundary conditions, and water injection Δp_w (the dimensions of the damaged elements and the aperture of the fracture are out of scale for schematization purposes)

4.2. Wetting test

Four samples with diameter $2R = 37\ mm$ and height $h = 40\ mm$ (see Fig. 11) collected from the U.A. were prepared and then fractured using the Brazilian splitting test. Sample preparation and experiments are described in [17], whose basic information is recalled in Tab. 4.

Tab. 4 Data on Callovo-Oxfordian samples used for the wetting test (from [17])

Sample label	*Core number*	*Depth (m)*	*Geological Unit*	*Saturation degree (%)*	*Initial aperture (μm)*
UA1-C	EST 57903	-490	UA	86.8	21.58
UA2-C	EST 58128	-490	UA	85.5	17.14
UA3-C1	EST 58145	-490	UA	84.3	16.02
UA3-C2	EST 58145	-490	UA	84.3	14.26

All samples are extracted from the same core and differ slightly from each other regarding the initial degree of saturation and initial fracture aperture. Synthetic water with specific mineralogical composition was prepared in the laboratory and then injected into the fracture, reaching the value of 0.5 MPa. Then, the drainage valve was closed, allowing the whole sample to be re-saturated. Since the injection duration is unknown, it is assumed in the following that the desired water pressure is reached in 3 hours, after which the fracture becomes saturated, and water begins to flow through the system. This choice is justified because, at least numerically, the injection duration does not affect the results.

4.2.1. Calibration of the hydro-mechanical parameters during wetting

In the following, the test UA2-C is described in detail to understand the physical meaning of the unknown parameters and how to use them to fit the experiments. As defined in Tab. 4, the initial fracture aperture for the test UA2-C is $d_{ini} = 21.58\ \mu m$. The corresponding thickness of the damaged sides is $h_{ini} = 11.4\ \mu m$ (see Fig. 5(b)).

A sensitivity analysis is performed to calibrate the penalty parameter $\widetilde{K}_N$ in Eq. (2) and the elastic coefficients κ_{el} in Eq. (14). In addition, the intrinsic transmissivity T_w controlling the transversal flow (Eqs. 8-9) should be defined. The values used for this sensitivity analysis are listed in Tab. 5.

Tab. 5 Parameters used for the sensitivity analysis during the wetting test UA2-C

Parameter	*Symbol (unit)*	*Value*
Elastic coefficients for the damaged sides	$\kappa_{el}\ (-)$	$[0;\ 0.55;\ 1.10; 2.20]$
Stiffness parameter	$\widetilde{K}_N\ (MPa\ m^{-1})$	[100; 400; 1000; 4000]
Intrinsic transmissivity	$T_w\ (m\ Pa^{-1}s^{-1})$	$[10^{-14};\ 10^{-15}; 10^{-16}]$

Fig. 12 shows the profile of water pressure p_w, effective normal pressure p'_n, and hydraulic opening d in the y-direction (i.e., along the fracture) when $\widetilde{K}_N = 400\ MPa/m$, $\kappa_{el} = 2.20$, and the absolute transmissivity is $T_w = 10^{-15}\ m/Pa\ s$. Three main phases can be observed:

i. $t \leq 3\ h$, injection phase: the pore water pressure increases along the whole fracture (y-direction) as shown in Fig. 12 (a); this corresponds to a slight reduction of the effective normal pressure (Fig. 12 (b)) and a slight increase of the fracture opening (Fig; 12 (c)); therefore this first part of the test is dominated by the resaturation of the fracture.

ii. $3\ h < t \leq 4\ days$, self-sealing phase: once the defined values of pore water pressure are reached on the top and the bottom of the fracture ($t = 3\ h$), a transient process is observed (Fig. 13). Water begins to flow transversely, firstly saturating the damaged area and then the rest of the sample. The two counterparts begin to swell, leading, by equilibrium, to the increase of the effective normal pressure within the fracture (Fig. 12 (b)) and consequently reducing its opening (Fig. 12 (c)). The variation in effective normal pressure p'_n and opening d along the fracture becomes more and more negligible until reaching a uniform trend along the y-direction after about 12 hours.

iii. $t > 4\ days$, stabilization. The pore water pressure reaches stationarity, as illustrated in Fig. 13. This result is consistent with Fig. 12 since, after 4 days, there is no significant temporal change in terms of effective pressure and fracture opening.

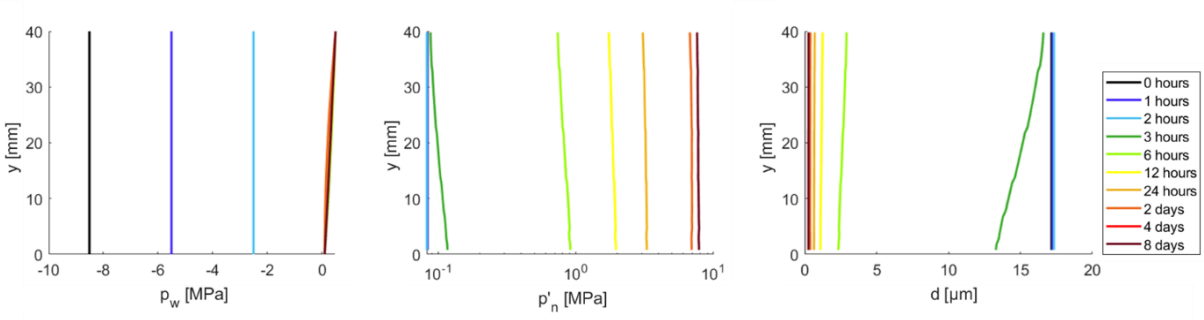

(a) (b) (c)

Fig. 12 Profiles of the main hydro-mechanical features obtained numerically along the fault opening for the UA2-C test ($\tilde{K}_N = 400\ MPa/m$, $\kappa_{el} = 2.20$ and $T_w = 10^{-15}\ m/Pa\ s$): (a) pore water pressure; (b) effective normal pressure; (c) fault opening (the legend is on the right for the three graphs)

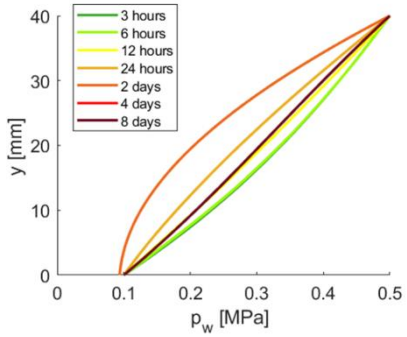

Fig. 13 Pore water pressure along the fault opening after the injection phase

Several numerical tests were carried out to quantify the effect of the elastic coefficient on self-sealing. The main results are plotted in Fig. 14 (a) in terms of the temporal evolution of the equivalent aperture. The figure also compares the numerical results with experiments. The initial opening (for $t \leq 3\ h$) is negligible compared to the following closure. Then, once the fracture saturates, it starts to close with time. This self-sealing process is not linear as it is rapid at the beginning, becoming slower and slower until stabilization at a constant final value (for $t = 4\ days$). These results are also consistent, at least qualitatively, with the trend observed experimentally [15], [17], [21], [22], [50]. Moreover, the increase in the elastic coefficient κ_{el} reduces the stiffness of the damaged sides (see Eq. (14)), thus increases their swelling and the closure of the fracture giving results comparable to experiments. An equivalent effect is obtained by varying the penalty coefficient $\tilde{K}_N$, as illustrated in Fig. 14 (b): the increase of the penalty increases the rigidity of the fracture, thus reducing its ability to seal. Considering the hydraulic properties, as already mentioned, the swelling of the rock depends on the ability of water to flow through it from the fracture; therefore, the transmissivity coefficient plays a predominant role, which is illustrated in Fig. 14 (c). It defines the rapidity of the hydraulic closure process: when $T_w = 10^{-16}\ m/Pa\ s$, the water flow is relatively slow, while $T_w \geq 10^{-15}$

$m/Pa\ s$ self-sealing is quick. In particular, $T_w = 10^{-14}\ m/Pa\ s$ gives a rapid reduction of the equivalent aperture that does not match experiments. The combination of parameters that seems to fit the experimental results best is given by $\widetilde{K}_N = 400\ MPa/m;\ \kappa_{el} = 2.20$ and $T_w = 10^{-15}\ m/Pa\ s$. These values will be used to validate the model against the other wetting tests presented in Tab. 4.

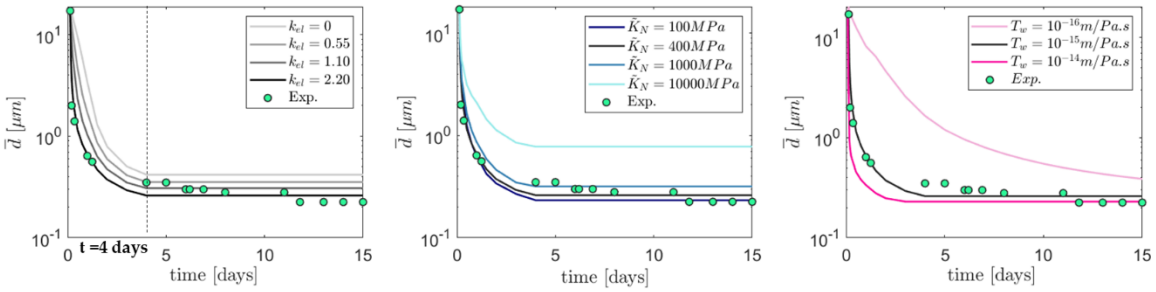

(a) (b) (c)

Fig. 14 Calibration of the hydromechanical parameters and comparison with the experimental test UA2-C: (a) effect of the elastic coefficient κ_{el} ($\widetilde{K}_N = 400\ MPa/m$ and $T_w = 10^{-14}\ m\ Pa^{-1}s^{-1}$); (b) effect of the stiffness coefficient $\widetilde{K}_N$ ($k_{el} = 2.20$ and $T_w = 10^{-14}\ m\ Pa^{-1}s^{-1}$); (c) effect of the absolute tramsissvity T_w ($k_{el} = 2.20$ and $\widetilde{K}_N = 400\ MPa/m$); the experimental data have been published in [17]

4.2.2. Results

The previously illustrated procedure is now adapted to the other samples of Tab. 4, and results are plotted in Fig. 15 regarding the temporal evolution of mean hydraulic opening compared with the experimental results. Based on the calibration performed in the previous Section 4.2.1, the following set of parameters is chosen: $\widetilde{K}_N = 400\ MPa/m;\ \kappa_{el} = 2.20$ and $T_w = 2\ 10^{-15}\ m/Pa\ s$, i.e., the same mechanical parameters used to obtain results in Fig. 12, while the intrinsic transmissivity T_w was slightly increased to find the best match for all the tests. As illustrated in Fig. 15, such parameters can fit the hydration tests successfully and reproduce self-sealing in the Callovo-Oxfordian claystone. It can be observed that the larger the initial fracture size, the smaller the sealing effect obtained.

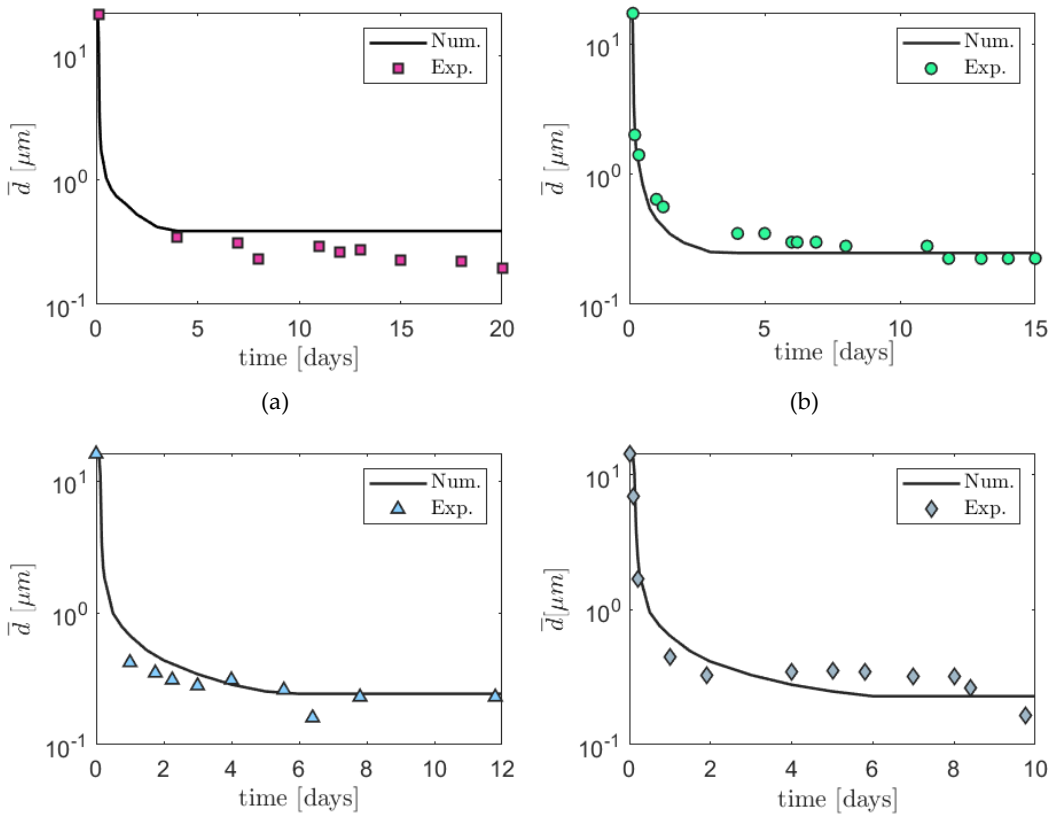

Fig. 15 Temporal evolution of the average fracture opening during the wetting test, comparison between numerical and experimental results obtained by [17]: (a) Test UA1-C; (b) Test UA2-C; (c) Test UA3-C1; (d) Test UA3-C2

A better understanding of the phenomena is achieved by observing the evolution of the water permeability with time. The equivalent fracture water permeability $\bar{k}_w^F$ is obtained by applying the cubic law in Eq. (13) to the equivalent fracture opening $\bar{d}$. However, it is generally more helpful to define the equivalent permeability for the entire sample cross-section, which is calculated as follows:

$$k_{w,eq} = \frac{A_{\Omega 1} k_{w1} + A_{\Omega 2} k_{w2} + A_F \bar{k}_w^F}{A_{tot}} \tag{20}$$

where $A_{\Omega 1}$and $A_{\Omega 2}$ are the surfaces of the two bulk elements, k_{w1} and k_{w2} the respective permeabilities, A_F is the surface of the fracture and A_{tot} is the surface of the whole sample.

Results are illustrated in Fig. 16. A good agreement between numerical and experimental results is also obtained in terms of equivalent permeability. It can be observed that the permeability of the intact material ($k = 1.33^{-20}\, m/s$, gray dot line in Fig. 16) is approached after the self-sealing process.

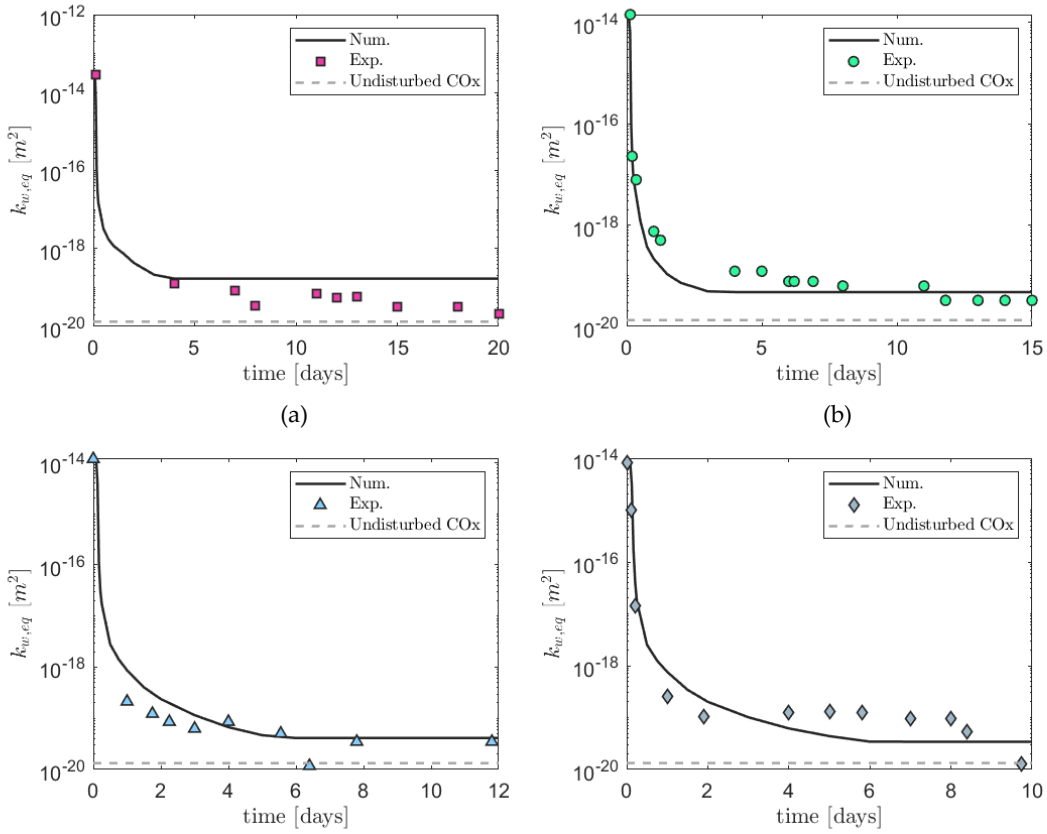

Fig. 16 Temporal evolution of the average equivalent permeability during the wetting test, comparison between numerical and experimental results obtained by [17]: (a) Test UA1-C; (b) Test UA2-C; (c) Test UA3-C1; (d) Test UA3-C2

4.3. Vapor - Wetting - Drying test

Another experimental campaign has been carried out by Di Donna and co-authors, as detailed in [16] and [21]. Cylindrical samples 8 mm in diameter and 20 mm in height were prepared and artificially fractured, as sketched in Fig. 11. The experimental setup consists in connecting the sample to a circuit that includes a pump and a reservoir. The sample defined in Tab. 6 was first saturated and then de-saturated. The saturation phase consists of injecting water vapor reaching relative humidity RH≈100 % and then liquid water, while desaturation occurs by injecting dry air (RH<20%). A sensor monitors the relative humidity and temperature inside the reservoir.

Tab. 6 Main feature of the wetting-drying test (from [21])

Sample label	*Core number*	*Depth (m)*	*Geological Unit*	*Water content (%)*	*Suction (MPa)*	*Initial aperture (μm)*
3132	EST 53644	-490	UA	6.2	14.3	75

4.3.1. Hydro-mechanical parameters

Due to its small size (8 millimeters in diameter), the sample is assumed to become slightly damaged during its preparation. Therefore, the Young modulus of the material is assumed to be 20 times lower than the one corresponding to the intact material.

Concerning the flow properties, vapor injection causes no significant effect on hydraulic closure for the duration of the experimental test [21]. Although the fracture becomes completely saturated, the vapor cannot quickly saturate the two adjacent clay elements as well. This evidence means that, contrary to what happens when liquid water is injected, the generation of secondary fractures on the sides of the main one is not clearly visible, and the swelling of clay minerals is minimal. However, the sample preparation and the creation of the main fracture, as well as the resaturation phase necessary to restore the sample to its in-situ condition (before starting the test), can induce some secondary cracks. This circumstance is considered in the model by accounting for a small thickness for the damaged sides ($h = 2\ \mu m$). Then water is injected into the fracture generating a well-defined weak zone around it, as illustrated previously in Fig. 5 ($h = 32\ \mu m$). The presence of a disturbed zone around the fracture also controls the subsequent drying phase.

The stiffness parameters for the interface element are assumed to be equal to those defined in the previous case independently from the fluid injected (i.e., they are properties of the material: $\widetilde{K}_N = 400\ MPa/m;\ \kappa_{el} = 2.20$).

Concerning the hydraulic parameters, a low transmissivity coefficient T_w is used to model the vapor phase to account for the fact that the closure by saturation by the vapor is slower than the one achieved by injecting liquid water. Here the intrinsic transmissivity is set to $T_w = 8e^{-18}\ m/Pa\ s$, while it is set to $2e^{-15}\ m/Pa\ s$ for the water and drying phases (the same value is used in previous wetting cases). For practical reasons, the gas supply phase is simulated by injecting air at very low relative humidity; therefore, the same intrinsic transmissivity value is used in wetting and drying. However, relative transmissivity (Eq. (10)) plays a fundamental role during drying since it considerably reduces the total transmissivity coefficient to values close to the transmissivity used during the vapor injection.

4.3.2. Results

The experimental and numerical evolution of the average fracture opening with time is plotted in Fig. 17(a). The three main stages of the test (i.e., vapor, water, and air) are visible both experimentally and numerically.

The vapor phase lasted about two days. An initial opening is observed experimentally that might indicate that the vapor phase is still not equilibrated [21]. Numerically, no initial opening is observed. Then, once saturation is achieved (relative humidity RH=1 in Fig. 17(a)), the fracture starts to close slowly.

The wetting phase is consistent with the tests discussed in the previous Section 4.2: the closure of the fracture is quite rapid at the beginning and then becomes slower and slower. Both experimentally and numerically, no effect is observed at the beginning of the drying phase, whereas a rapid increase in the hydraulic opening is observed experimentally after about four

days. Numerically the process starts slightly later. However, the final opening value achieved in the model is comparable with the one obtained from the test. The mismatch between numerical and experimental results during the drying phase can be due to the assumption made in the numerical model (e.g., the drying is simulated by injecting water at negative pressure).

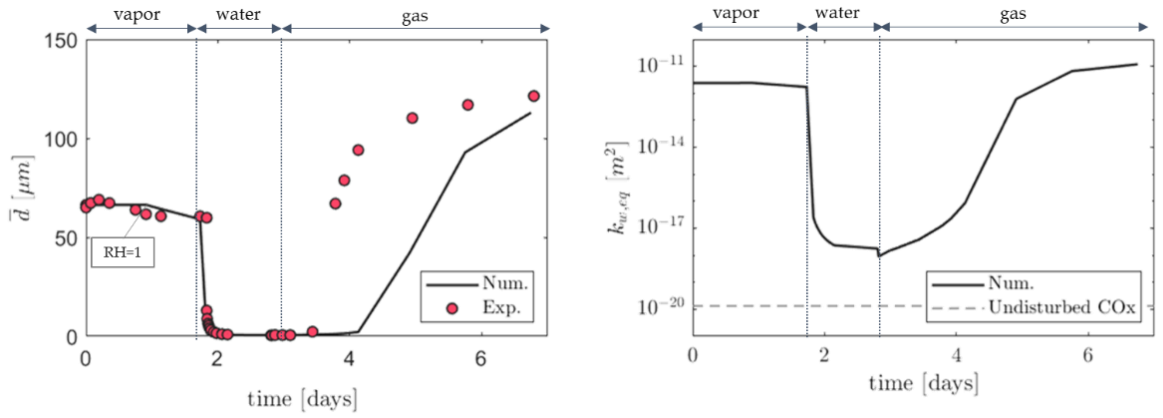

(a) (b)

Fig. 17 Temporal evolution of the average fault opening during test 3132; the experimental results refer to [17]; (b) equivalent water permeability during test 3132

Since the permeability was not measured experimentally, the comparison can only be performed regarding fracture opening. However, the cubic law allows the computation of the fracture permeability, from which it is possible to estimate the equivalent permeability for the whole sample, as defined in Eq. (20). Results are illustrated in Fig. 17(b). During the wetting phase, the equivalent permeability reaches the value $k_{w,eq} \cong 1\ 10^{-18} m^2$ that is still larger than the value of the undisturbed rock and those computed in Section 4.2. This result can be related to the size of the fracture that is larger in this test than in the previous case study; in fact, it was observed that the larger the fracture opening, the smaller the sealing effect.
The hydraulic closure/opening of the fracture is driven by the swelling/contraction of the clay minerals from the lips of the fracture itself towards the sample boundaries.

4.4. Drying - Wetting test

In the experimental campaign published in [21] and introduced in Section 4.3, other tests were carried out by injecting first some dry air and then re-saturating with liquid water. The test selected in this study is the n. 8182, extracted from the same core of the test n. 3132 described in Tab. 6. Therefore, it has the same initial features as the previous one, except for the initial fracture size, which is 285 μm for the present case study. As for the test n. 3132, due to its small size, the Young modulus is reduced due to the preparation induced damage ($E = 200\ MPa$) with respect to the one of the undisturbed material.

4.4.1. *Hydro-mechanical parameters*

If the sample is firstly de-saturated, the drying does not induce any visible damage around the discontinuity, at least for the duration of the considered experimental test. Then, the hydration generates a well-defined damaged area around the fracture.

Through the power law in Fig. 5 (b), it is possible to compute the thickness of the damaged sides during hydration ($h = 122\ \mu m$). The same mechanical and hydraulic parameters defined in Sections 4.2-4.3 are used for this numerical test.

4.4.2. *Results*

The experimental and numerical variations of the fracture opening with time are displayed in Fig. 18. Numerically, the aperture varies almost linearly with time.

The hydration phase generates secondary cracks around the primary discontinuity that favor the hydraulic closure of the fracture: the opening $\bar{d}$ decreases very quickly at first and then more and more slowly, in line with what was discussed above in Sections 4.2 and 4.3. The same trend is observed numerically.

The final equivalent water permeability reached (Fig. 18 (b)) is a few orders of magnitude higher than the permeability of the intact material.

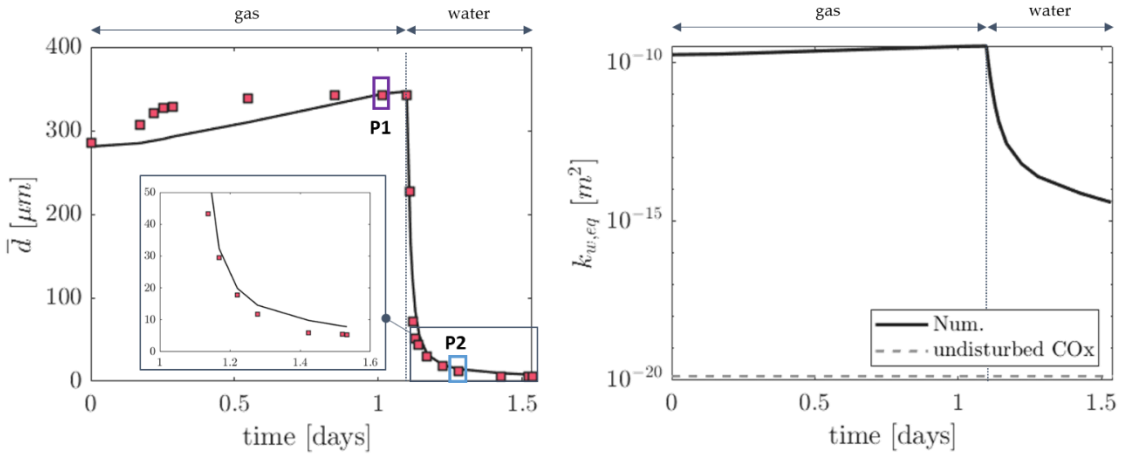

Fig. 18 Temporal evolution of: (a) the average fault opening $\bar{d}$ during test 8182; the experimental results refer to [17] (points P1 and P2 will be reminded in Fig. 19) (b) equivalent permeability $k_{w,eq}$

Although the temporal evolution of the opening during drying does not follow the same behavior observed experimentally, there is a good match at the end of this phase. This aspect is confirmed by observing the displacement field in Fig. 19 corresponding to point P1 in Fig. 18. Afterward, almost at the end of the re-saturation process (point P2 in Fig. 18), a good match between numerical and experimental displacement is observed in the whole section of the sample. The large displacements computed numerically close to the fracture (light blue zone in Fig. 19) are related to the damage generated around it, as already observed in Fig. 5 (a).

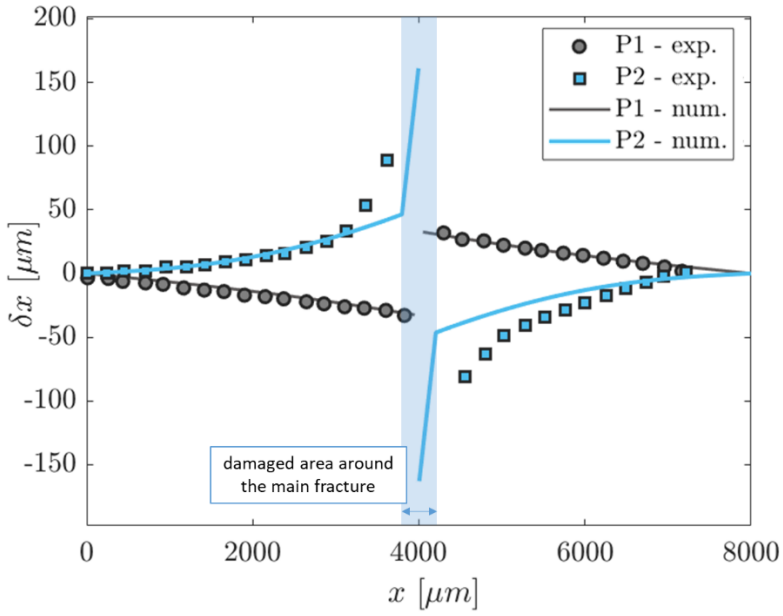

Fig. 19 Gradient of displacements for a section in the middle of the sample and along the x-direction of dry air (point P1 in Fig. 19) and water (point P2 in Fig. 18)

5. Discussion

The saturation phase generates micro-cracks around the fracture, defining a low-density and fairly compressible zone, which is even more evident the greater the initial size of the fracture. Thanks to the clay transmissivity, the water injected can permeate the clay, first involving the damaged zone and then the rest of the sample. This process is clearly demonstrated by both numerical and experimental results. However, the bigger the initial crack, the lower the recovery.

Fig. 20 shows the final fracture aperture d_f against the initial one d_{ini}. It is fairly straightforward to see that the model is capable of reproducing the self-sealing well for a low initial aperture d_{ini}. However, the 3132 and 8182 tests, corresponding to high initial aperture value, are more complex, as they include a vapor and gas injection phase in addition to the saturation phase with water. These phases were reproduced numerically by controlling the water pressure in the fracture and without taking into account the real nature and the chemical composition of the fluid injected, thus could explain the slight offset from the experimental results.

The fracture closure dramatically reduces the water permeability, reaching values close to the intact material.

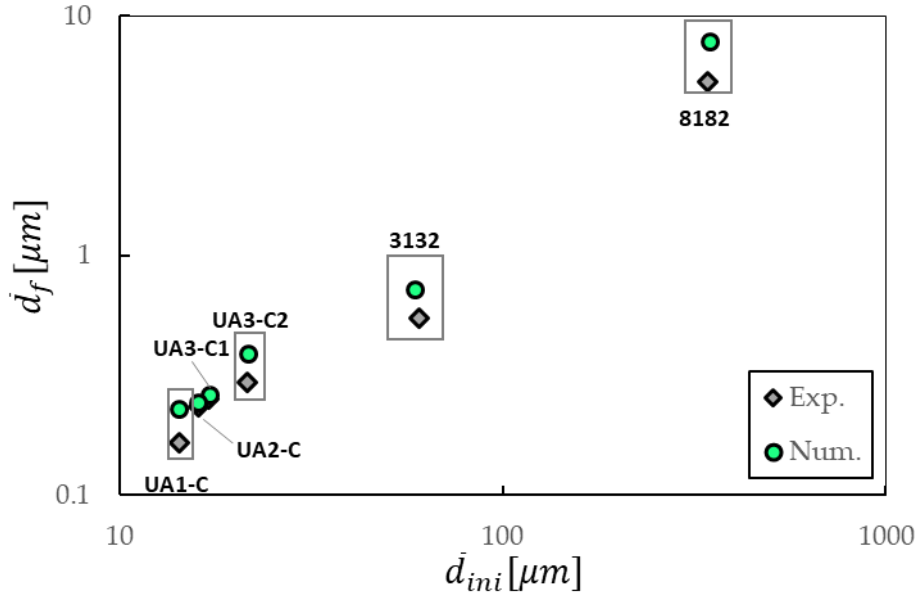

Fig. 20 Variation of the averaged final fracture d_f as a function of the initial value d_{ini}

6. Conclusions

The numerical model, together with the calibration of the mechanical and hydraulic parameters, is able to well reproduce the self-sealing of clay materials at the scale of laboratory tests in terms of fracture closure and water permeability. The latter is assumed to be related to the fracture opening through the cubic law.

Both experimentally and numerically, once the fracture is saturated, the recovery takes place first quickly thanks to the swelling of clay minerals close to the fracture where some microcracks generate, defining preferential paths for the water migration, and then slowly until stabilization is reached. Here the permeability reaches a value close to the intact material. Recovery is generally successfully achieved for a small initial opening of the fracture. The recovery obtained by vapor saturation is negligible, but it is thought to be related to the short duration of the considered experiments. In this sense, it might be interesting to carry out longer tests.

The drying phase leads to different results depending on whether it follows or precedes hydration: in the first case, hydration leads to a clearly visible cracked area around the fracture which can contract during drying, favoring hydraulic opening, while in the second case, a slight opening is observed since the secondary cracks are absent or not visible at the beginning of the test and are not generated by the drying. This behavior is considered in the numerical modeling, and the results agree with the experiments. However, for the test n. 3132, the experimental results are not so well reproduced in terms of the fracture opening rate. As mentioned, this difference can be caused by the assumption in gas injection modeling. Moreover, the undisturbed material is assumed elastic, which simplifies the reality strongly. It is worth recalling that this study is focused on the self-sealing of the fracture and, thus, on the recovery of hydraulic properties during the hydration phase. The vapor and gas injection

phases have been simplified since the gas pressure is kept constant to the environmental value. Moreover, additional experimental tests are necessary to further investigate the fluid exchanges during these phases.
Nevertheless, horizontal displacements are uniform along the vertical direction, which is consistent with what was observed experimentally.
To further validate the model, the interface constitutive equations can be employed to test other materials and ultimately to predict self-sealing at a large scale (i.e., *in-situ* experiments). Moreover, since the model is developed in 2D, it does not account for any material anisotropy, which can play an important role in self-sealing.

Acknowledgments

This research was supported by the University of Liège under Special Funds for Research, IPD-STEMA Programme. This work was also carried out in the framework of the EURAD, European Joint Programme on Radioactive Waste Management (under grant agreement No 847593), to which the authors are grateful.

7. References

[1] Les recherches de l'Andra sur le stockage géologique des déchets radioactifs à haute activité et à vie longue-Résultats et perspectives," ANDRA Dossier 2005..

[2] F. Bernier et al., "SELFRAC: fractures and self-healing within the excavation disturbed zone in clays. Final report. EURIDICE Report," 2007.

[3] C. F. Tsang, F. Bernier, and C. Davies, "Geohydromechanical Processes in the Excavation Damaged Zone in Crystalline Rock, Rock Salt," Int. J. Rock Mech. Min. Sci., no. June, 2004.

[4] G. Armand, F. Leveau, C. Nussbaum, R. de la Vaissiere, A. Noiret, D. Jaeggi, P. Landrein & C. Righini, "Geometry and properties of the excavation-induced fractures at the meuse/haute-marne URL drifts," Rock Mech. Rock Eng., vol. 47, no. 1, pp. 21–41, Jan. 2014, doi: 10.1007/s00603-012-0339-6.

[5] B. Pardoen, J. Talandier, and F. Collin, "Permeability evolution and water transfer in the excavation damaged zone of a ventilated gallery," Int. J. Rock Mech. Min. Sci., vol. 85, no. May, pp. 192–208, 2016, doi: 10.1016/j.ijrmms.2016.03.007.

[6] H. Bock et al., Self-sealing of fractures in argillaceous formations in the context of geological disposal of radioactive waste : review and synthesis. OECD, 2010.

[7] J. Delay, A. Vinsot, J.-M. Krieguer, H. Rebours, and G. Armand, "Making of the underground scientific experimental program at the Meuse/Haute-Marne underground research laboratory, North Eastern France," Phys. Chem. Earth, Parts A/B/C, vol. 32, pp. 2–18, Dec. 2007, doi: 10.1016/j.pce.2006.04.033.

[8] J. Mayor, J. García-Siñeriz, E. E. Alonso, H. Alheid, and P. Blümling, "Engineered barrier emplacement experiment in Opalinus Clay for the disposal of radioactive waste

in underground repositories," ENRESA Empres. Nac. Residuos Radiact., no. March 2017, pp. 1–101, 2005.

[9] W. Bastiaens, F. Bernier, and X. L. Li, "SELFRAC: Experiments and conclusions on fracturing, self-healing and self-sealing processes in clays," Phys. Chem. Earth, vol. 32, no. 8–14, pp. 600–615, 2007, doi: 10.1016/j.pce.2006.04.026.

[10] M. Van Geet, W. Bastiaens, and L. Ortiz, "Self-sealing capacity of argillaceous rocks: Review of laboratory results obtained from the SELFRAC project," Phys. Chem. Earth, vol. 33, no. SUPPL. 1, 2008, doi: 10.1016/j.pce.2008.10.063.

[11] R. de la Vaissière, G. Armand, and J. Talandier, "Gas and water flow in an excavation-induced fracture network around an underground drift: A case study for a radioactive waste repository in clay rock," J. Hydrol., vol. 521, pp. 141–156, 2015, doi: 10.1016/j.jhydrol.2014.11.067.

[12] R. de la Vaissière, G. Armand, and J. Talandier, "Excavation damaged zone under imbibition: Evidence of self-sealing into claystone," Unsaturated Soils Res. Appl. - Proc. 6th Int. Conf. Unsaturated Soils, UNSAT 2014, vol. 2, pp. 1481–1487, 2014, doi: 10.1201/b17034-216.

[13] C. A. Davy, F. Skoczylas, J. D. Barnichon, and P. Lebon, "Permeability of macro-cracked argillite under confinement: Gas and water testing," Phys. Chem. Earth, vol. 32, no. 8–14, pp. 667–680, 2007, doi: 10.1016/j.pce.2006.02.055.

[14] C. L. Zhang, "Sealing of fractures in claystone," J. Rock Mech. Geotech. Eng., vol. 5, no. 3, pp. 214–220, 2013, doi: 10.1016/j.jrmge.2013.04.001.

[15] R. Giot, C. Auvray, and J. Talandier, "Self-sealing of claystone under x-ray nanotomography," Geol. Soc. Spec. Publ., vol. 482, no. 1, pp. 213–223, 2019, doi: 10.1144/SP482.4.

[16] A. Di Donna, P. Charrier, S. Salager, and P. Bésuelle, "Self-sealing capacity of argillite samples," 2020. [Online]. Available: https://hal.archives-ouvertes.fr/hal-02012618.

[17] C. Wang, J. Talandier, and F. Skoczylas, "Swelling and Fluid Transport of Re-sealed Callovo–Oxfordian Claystone," Rock Mech. Rock Eng., vol. 55, no. 3, pp. 1143–1158, 2022, doi: 10.1007/s00603-021-02708-4.

[18] C. L. Zhang and J. Talandier, "Self-sealing of fractures in indurated claystones measured by water and gas flow," J. Rock Mech. Geotech. Eng., no. xxxx, pp. 1–14, 2022, doi: 10.1016/j.jrmge.2022.01.014.

[19] N. Conil et al., "How rock samples can be representative of in situ condition: A case study of Callovo-Oxfordian claystones," J. Rock Mech. Geotech. Eng., vol. 10, no. 4, pp. 613–623, 2018, doi: 10.1016/j.jrmge.2018.02.004.

[20] B. Yven and S. Sammartino, "Mineralogy, texture and porosity of Callovo-Oxfordian argillites of the Meuse/Haute-Marne region (eastern Paris Basin)," Bulletin de la Societe Geologique de France. Mém. Soc. géol. France,. 73-90.

[21] A. Di Donna, P. Charrier, J. Dijkstra, E. Andò, and P. Bésuelle, "The contribution of swelling to self-sealing of claystone studied through x-ray tomography," Phys. Chem. Earth, vol. 127, no. June, 2022, doi: 10.1016/j.pce.2022.103191.

[22] H. Wang, Y. J. Cui, M. N. Vu, J. Talandier, and N. Conil, "Fracture effect on the hydro-mechanical behaviour of Callovo-Oxfordian claystone," Eng. Geol., vol. 303, no. April, p. 106674, 2022, doi: 10.1016/j.enggeo.2022.106674.

[23] H. Wang, R. de La Vaissière, M. N. Vu, C. La Borderie, and D. Gallipoli, "Numerical modelling and in-situ experiment for self-sealing of the induced fracture network of drift into the Callovo-Oxfordian claystone during a hydration process," Comput. Geotech., vol. 141, Jan. 2022, doi: 10.1016/j.compgeo.2021.104487.

[24] R. Charlier, "Approche unifiée de quelques problèmes non linéaires de mécanique des milieux continus par la méthode des éléments finis (grandes déformations des métaux et des sols, contact unilatéral de solides, conduction thermique et écoulements en milieu poreux)," Université de Liège, Belgium, 1987.

[25] F. Collin, "Couplages thermo-hydro-mécaniques dans les sols et les roches tendres partiellement saturés. Thèse de Doctorat. Université de Liège, Belgique, 300p.," p. 300, 2003.

[26] R. E. Goodman, R. L. Taylor, and T. L. Brekke, "A Model for the Mechanics of Jointed Rock," J. Soil Mech. Found. Div., vol. 94, no. 3, pp. 637–659, May 1968, doi: 10.1061/JSFEAQ.0001133.

[27] R. Charlier and S. Cescotto, "Modelisation du phenomene de contact unilateral avec frottement dans un contexte de grandes deformations," Journal de mecanique theorique et appliquee, vol. 7, no. 1. pp. 177–192, 1988.

[28] R. A. Day and D. M. Potts, "Zero thickness interface elements—numerical stability and application," Int. J. Numer. Anal. Methods Geomech., vol. 18, no. 10, pp. 689–708, Oct. 1994, doi: https://doi.org/10.1002/nag.1610181003.

[29] B. Cerfontaine, A. C. Dieudonné, J. P. Radu, F. Collin, and R. Charlier, "3D zero-thickness coupled interface finite element: Formulation and application," Comput. Geotech., vol. 69, pp. 124–140, Sep. 2015, doi: 10.1016/j.compgeo.2015.04.016.

[30] A. M. Habraken and S. Cescotto, "Contact between deformable solids: The fully coupled approach," Math. Comput. Model., vol. 28, no. 4–8, pp. 153–169, 1998, doi: 10.1016/S0895-7177(98)00115-0.

[31] M. A. Puso and T. A. Laursen, "A mortar segment-to-segment contact method for large deformation solid mechanics," Comput. Methods Appl. Mech. Eng., vol. 193, no. 6, pp. 601–629, 2004, doi: https://doi.org/10.1016/j.cma.2003.10.010.

[32] K. A. Fischer and P. Wriggers, "Mortar based frictional contact formulation for higher order interpolations using the moving friction cone," Comput. Methods Appl. Mech. Eng., vol. 195, no. 37, pp. 5020–5036, 2006, doi: https://doi.org/10.1016/j.cma.2005.09.025.

[33] S. C. Bandis, A. C. Lumsden, and N. R. Barton, "Fundamentals of rock joint deformation," Int. J. Rock Mech. Min. Sci. Geomech. Abstr., vol. 20, no. 6, pp. 249–268, 1983, doi: https://doi.org/10.1016/0148-9062(83)90595-8.

[34] A. Gens, I. Carol, and E. E. Alonso, "A constitutive model for rock joints formulation and numerical implementation," Comput. Geotech., vol. 9, no. 1, pp. 3–20, 1990, doi: https://doi.org/10.1016/0266-352X(90)90026-R.

[35] M. E. Plesha, "Rock joints: Theory, constitutive equations," in Mechanics of Geomaterial Interfaces, vol. 42, A. P. S. Selvadurai and M. J. B. T.-S. in A. M. Boulon, Eds. Elsevier, 1995, pp. 375–393.

[36] S. Gentier, C. Petitjean, J. Riss, and G. Archambault, "Hydromechanical behavior of a natural joint under shearing," 2nd North Am. Rock Mech. Symp. NARM 1996, no. January, pp. 1201–1208, 1996.

[37] M. Bart, J. F. Shao, D. Lydzba, and M. Haji-Sotoudeh, "Coupled hydromechanical modeling of rock fractures under normal stress," Can. Geotech. J., vol. 41, no. 4, pp. 686–697, Aug. 2004, doi: 10.1139/T04-018.

[38] F. Salehnia, X. Sillen, X. L. Li, and R. Charlier, "Numerical simulation of a discontinuous gallery lining's behavior, and its interaction with rock," Int. J. Numer. Anal. Methods Geomech., vol. 41, no. 15, pp. 1569–1589, Oct. 2017, doi: 10.1002/nag.2689.

[39] C. Guiducci, F. Collin, J. P. Radu, A. Pellegrino, and R. Charlier, "Numerical modeling of Hydro-Mechanical fracture behavior ISRM 2003-Technology roadmap for rock mechanics," pp. 1–6, 2003.

[40] M. T. van Genuchten, "A Closed-form Equation for Predicting the Hydraulic Conductivity of Unsaturated Soils," Soil Sci. Soc. Am. J., vol. 44, no. 5, pp. 892–898, Sep. 1980, doi: https://doi.org/10.2136/sssaj1980.03615995004400050002x.

[41] M. Nuth and L. Laloui, "Effective stress concept in unsaturated soils: Clarification and validation of a unified framework," Int. J. Numer. Anal. Methods Geomech., vol. 32, no. 7, pp. 771–801, May 2008, doi: https://doi.org/10.1002/nag.645.

[42] Y. W. Tsang and P. A. Witherspoon, "Hydromechanical behavior of a deformable rock fracture subject to normal stress," J. Geophys. Res. Solid Earth, vol. 86, no. B10, pp. 9287–9298, Oct. 1981, doi: https://doi.org/10.1029/JB086iB10p09287.

[43] A. P. Oron and B. Berkowitz, "Flow in rock fractures: The local cubic law assumption reexamined," Water Resour. Res., vol. 34, no. 11, pp. 2811–2825, 1998, doi: 10.1029/98WR02285.

[44] R. Olsson and N. Barton, "An improved model for hydromechanical coupling during shearing of rock joints," Int. J. Rock Mech. Min. Sci., vol. 38, no. 3, pp. 317–329, 2001, doi: https://doi.org/10.1016/S1365-1609(00)00079-4.

[45] K. H. Roscoe and J. Burland, "On the Generalized Stress-Strain Behavior of Wet Clays," Jan. 1968.

[46] R. Charlier, F. Collin, B. Pardoen, J. Talandier, J. P. Radu, and P. Gerard, "An unsaturated hydro-mechanical modelling of two in-situ experiments in Callovo-Oxfordian argillite," Eng. Geol., vol. 165, pp. 46–63, Oct. 2013, doi: 10.1016/j.enggeo.2013.05.021.

[47] G. Armand, N. Conil, J. Talandier, and D. M. Seyedi, "Fundamental aspects of the hydromechanical behaviour of Callovo-Oxfordian claystone: From experimental studies to model calibration and validation," Comput. Geotech., vol. 85, pp. 277–286, 2017, doi: 10.1016/j.compgeo.2016.06.003.

[48] R. Charlier, F. Collin, B. Pardoen, J. Talandier, J. P. Radu, and P. Gerard, "An unsaturated hydro-mechanical modelling of two in-situ experiments in Callovo-Oxfordian argillite," Eng. Geol., vol. 165, pp. 46–63, 2013, doi: 10.1016/j.enggeo.2013.05.021.

[49] S. Levasseur, F. Collin, K. Daniels, M. Dymitrowska, J. Harrington, E. Jacops, O. Koldits, P. Marschall, S. Norris, X. Sillen, J. Talandier, L. Truche, and J. Wendling, 2020 "Initial state of the Art on Gas Transport in clayey Materials", Deliverable D6.1 in the HORIZON 2020 project EURAD, Work Package GAS. EC Grant agreement no: 847593

[50] F. Zhang, Y. J. Cui, N. Conil, and J. Talandier, "Assessment of Swelling Pressure Determination Methods with Intact Callovo-Oxfordian Claystone," Rock Mech. Rock Eng., vol. 53, no. 4, pp. 1879–1888, Apr. 2020, doi: 10.1007/s00603-019-02016-y.